scientific reports

OPEN

N-Cadherin based adhesion and Rac1 activity regulate tension polarization in the actin cortex

Seyedsajad Moazzeni[1,2], Kelly Kyker-Snowman[2], Rick I. Cohen[2], Huan Wang[3], Ran Li[1], David I. Shreiber[2], Jeffrey D. Zahn[2], Zheng Shi[3✉] & Hao Lin[1✉]

Tension-adhesion interplay is a crucial mechanism in multicellular organisms that determines the tension differential among internal and external interfaces, which in turn, mediates tissue surface tension and cell sorting, morphogenesis and remodeling, and cancer progression. Cadherins are widely believed to be involved, yet key aspects of the process are neither well characterized nor quantified. This study demonstrates the critical role of N-cadherin in driving tension polarization throughout the actin cortical network. N-cadherin regulates both tension increase at the cell-medium (external) interface and decrease at the cell-cell (internal) interface, and their quantitative magnitudes, both absolute and relative, strongly depend on the surface density of N-cadherin. Furthermore, the strength of tension polarization also increases with respect to the number of cell-cell interfaces for cells within a multicellular cluster. The cadherin-actin contractility linkage is mediated by Rac1, which serves as a molecular switch to trigger cortex remodeling and contraction via myosin II. Inhibition of Rac1 activity decreases tension polarization and leads to reduced coherence in both small clusters and spheroids. These results provide a pathway to reconcile opposing theories for tissue surface tension generation and perspectives in cancer treatment.

Cortical tension and cell-cell adhesion are a closely-connected pair of physical forces that play crucial roles in the organization of multicellular aggregates and tissues, and in biological processes such as embryogenesis, morphogenesis, cancer metastasis, and wound healing[1–8]. For example, they determine "tissue surface tension" (TST) which in turn directs embryonic cell sorting[9]. A balance between the two sets the "right" structural strength and pliancy to allow circulating tumor cell clusters, a more malignant form of the metastatic invasion when compared with single circulating cells, to translocate through narrow constrictions without occlusion or breaking apart[10]. Their competition in the cellular energy landscape dictates if a confluent tissue is in a "solid" or "fluid" regime, the former showing jamming effects, whereas the latter facilitates collective migration[11,12]. The tension-adhesion interplay is of fundamental significance in determining the mechanical behavior of cells in broad physiological and pathophysiological scenarios.

For decades, researchers have debated opposing theories that identify either tension or adhesion as the driving force in directing multicellular organization and developmental processes. The Differential Adhesion Hypothesis (DAH[13,14]) suggests that adhesive energy of cell adhesion molecules is the primary determinant of the TST, whereas the Differential Interfacial Tension Hypothesis (DITH[15,16]), as its name suggests, emphasizes the contribution of cellular tension differential. Recent advances have revealed more complex, dynamic co-action of the two[17–20], and their crosstalk at the molecular level[21–26]. Some studies focused on the role of cadherins in adhesive strength[27–29]. However, others found cadherin contributions via binding energy negligible[17,19,30]; instead, cadherins support contact formation through signaling for tension modification at cell-cell contacts[28,31]. Amack and Manning further advanced these ideas and suggested that cells on the boundaries "mechanically polarize" through cadherin signaling, leading to a tension differential along internal and external interfaces[32]. These effects had been directly observed in blastomeres in compacting mouse embryos and indirectly indicated in other studies both in vitro and in vivo, e.g., for cells and zebrafish development models[33–35]. However, as a key

[1]Department of Mechanical & Aerospace Engineering, Rutgers, The State University of New Jersey, 98 Brett Rd, Piscataway, NJ 08854, USA. [2]Department of Biomedical Engineering, Rutgers, The State University of New Jersey, 599 Taylor Rd, Piscataway, NJ 08854, USA. [3]Department of Chemistry and Chemical Biology, Rutgers, The State University of New Jersey, 123 Bevier Rd, Piscataway, NJ 08854, USA. ✉email: zheng.shi@rutgers.edu; hlin@soe.rutgers.edu

aspect of this tension differential, the tension increase at the cell-medium (external) interface appears to be "cell-autonomous" and not mediated by E-cadherin (Cdh1) nor adhesion in general, as suggested by Maître et al.[34].

Herein, we propose that N-cadherin (Cdh2) based adhesion is capable of regulating mechanical polarization by *both* mediating the tension increase at the cell-medium (external) interface and the decrease at the cell-cell (internal) interface, leading to tension polarization[1]. Further, the cadherin-actin contractility molecular linkage is proposed to be mediated by Rac1. To validate these hypotheses, we employ L929 cells transduced with LifeAct-mRuby2 and N-cadherin-EGFP, with the latter expressed at three distinct levels (LAN-High, LAN-Med, and LAN-Low). The L929 cell line was selected due to the lack of endogenous cadherin expression (hence adhesion-based coupling[14,36]) in the wild type and displaying constant active cortical layer under the plasma membrane in suspension, making them ideal cell type not only for studying the role of adhesion molecules in cell adhesion and developmental processes, but also for monitoring changes in the cortical layer[9,14,18,36–41]. We combine mechanical analysis by micropipette aspiration with direct F-actin and N-cadherin imaging to perform an in-depth, systematic examination of tension-adhesion coupling in relation to tension polarization. Particularly, different N-cadherin expression levels from low to high allow quantitative characterization of the correlation between tension and adhesion, which has been essentially absent from prior studies. We begin with doublets and then expand the study to greater numbers of interacting cells while using single cells as control. The molecular linkage is interrogated via various pharmacological treatments, and their effects are also examined in a spheroid growth model.

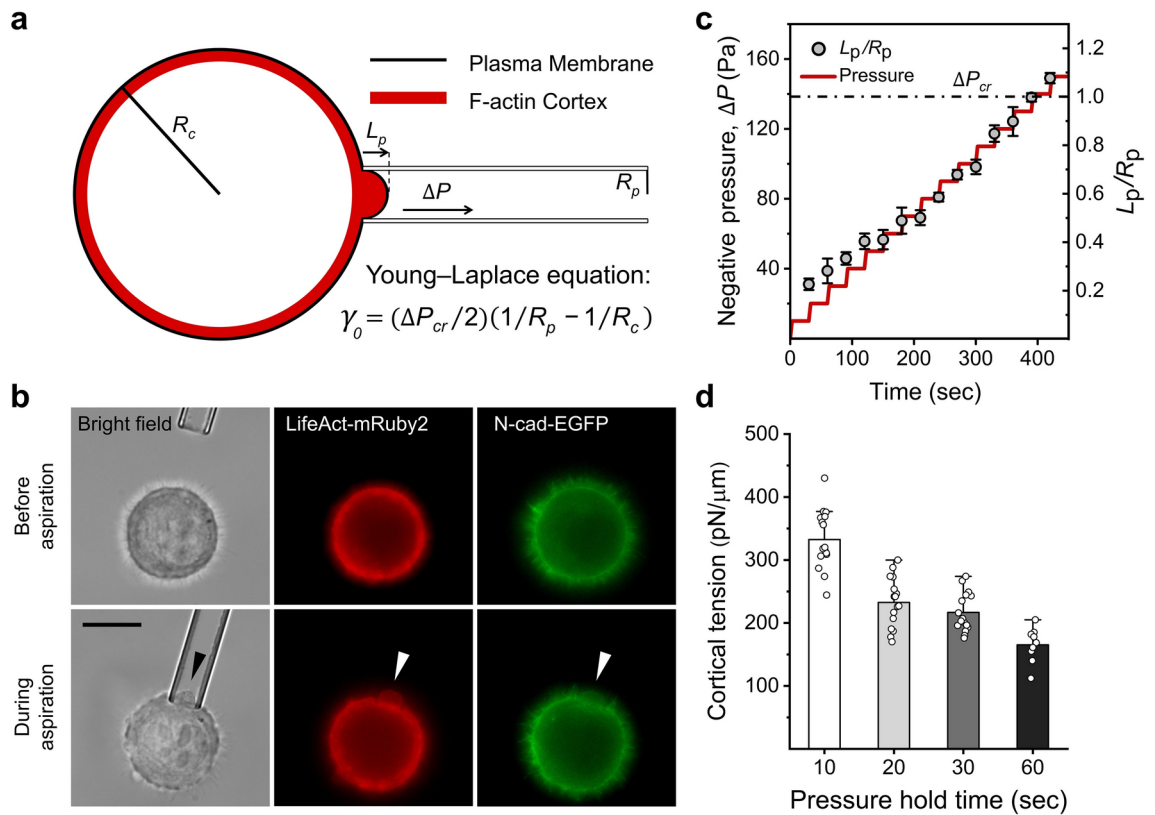## Results

Cortical tension quantification

Figure 1 summarizes our approach and the cortical tension measurement results using high N-cadherin expressing cells (LAN-High) as an example. We demonstrate the process with single suspended cells, and measurements for multiple adhered cells follow the same protocol. Tension is quantified via the Young-Laplace equation following pipette aspiration (Fig. 1a,b). The LAN-High cells express both LifeAct-mRuby2 and EGFP-tagged N-cadherin (with $3.2 \pm 0.6 \times 10^5$ surface molecules per cell, see Methods). Fluorescently-labeled cadherin and actin improved visualization of cortical deformation and enabled recording and analysis of the aspiration process in bright field, RFP, and GFP channels (Fig. 1b). To establish a tension quantification protocol, aspiration pressure was increased in 10 Pa increments and held for various durations (10, 20, 30, or 60 sec) until the cortex protrusion length into the pipette, L_p, equalled the radius of the pipette, R_p. An example of the aspiration pressure profile for a 30-sec hold time and the corresponding evolution in cortical deformation is shown in Fig. 1c. Once the condition $L_p/R_p = 1$ is met, cortical tension γ_0 is computed with the Young-Laplace equation, $\gamma_0 = (\Delta P_{cr}/2)(1/R_p - 1/R_c)$, where ΔP_{cr} is the pressure reached at $L_p = R_p$, and R_c is cell radius. The resulting γ_0 values for different hold times are shown in Fig. 1d. Measured tension for briefer aspiration (10-sec hold time) was greater when compared with all other groups, whereas relatively longer aspirations (60-sec hold time) resulted in significantly lower measured values, in agreement with previous studies demonstrating the time-dependent behavior of actin cortex[42–44]. We observed spontaneous membrane elongation and rupture in some cases with hold times shorter than or equal to 20 sec[45,46], and plastic deformation of the actin cortex with the 60-sec hold time (data not presented). On the other hand, these structural alterations were absent for the 30-sec hold time, and this hold time was chosen for all ensuing measurements in this study[40,47,48].

N-cadherin-based cell adhesion leads to tension polarization

We interrogated the co-action of tension and adhesion by performing cortical tension measurements on doublets with mature adhesion. A doublet is a pair of cells bound via adhesion and represents the ideal, minimal unit for observing this co-action. To examine the cortical tension regulation introduced by cell-cell adhesion, we performed measurements on the three subclones of the L929 cell line engineered and selected to express varying levels of N-cadherin-EGFP molecules per cell (LAN-High, LAN-Med, and LAN-Low; see Methods), which was expected to modulate the strength of adhesion. Figure 2a illustrates the gradient of N-cadherin-EGFP expression among these subclones, while actin (labeled with LifeAct-mRuby2) is equally expressed (see Fig. S3 and Table 3 for a detailed quantification of N-cadherin expression levels). Cortical tension was quantified for all three cell lines for both suspended single cells (γ_0) and doublets (γ_{cm}, where the subscript "cm" denotes cell-medium interface) 1 hour after initial cell-cell adhesion (Fig. 2b). The interfacial tension (γ_{cc}, where the subscript "cc" denotes cell-cell interface) was calculated for doublets using the measured contact angle (θ) and the Young-Dupré equation, $\gamma_{cc} = \gamma_{cm} \cos \theta$ (Fig. 2c).

A significant increase in cortical tension was measured in doublets compared to single cells (Fig. 2d). The increase in cortical tension from singles cells to doublets was significant for both high- and medium-expressing cells (LAN-High, $p < 0.001$; LAN-Med, $p < 0.01$), but not for low-expressing cells (LAN-Low, $p = 0.72$). In comparison, no significant differences in cortical tension were found among single cells of all the subclones (ANOVA, $p = 0.24$), which is expected. These results demonstrate that increased cortical tension in doublets is induced by N-cadherin-based adhesion. On the other hand, the calculated interfacial tension, γ_{cc}, decreases from γ_0. Notably, an approximately linear correlation is observed between the cortical tension and contact angle in doublets, as demonstrated in Fig. 2f. When applied to the Young-Dupré equation to calculate the interfacial tension (Fig. 2c), the resulting γ_{cc} values across different subclones do not result in statistical difference (Fig. 2e, ANOVA, $p = 0.25$), demonstrating a trend toward interfacial tension homeostasis among subclones with varying levels of N-cadherin expression.

---

[1] To avoid confusion with the widely used terminology of cellular polarization, we employ the specific term of 'tension polarization'.
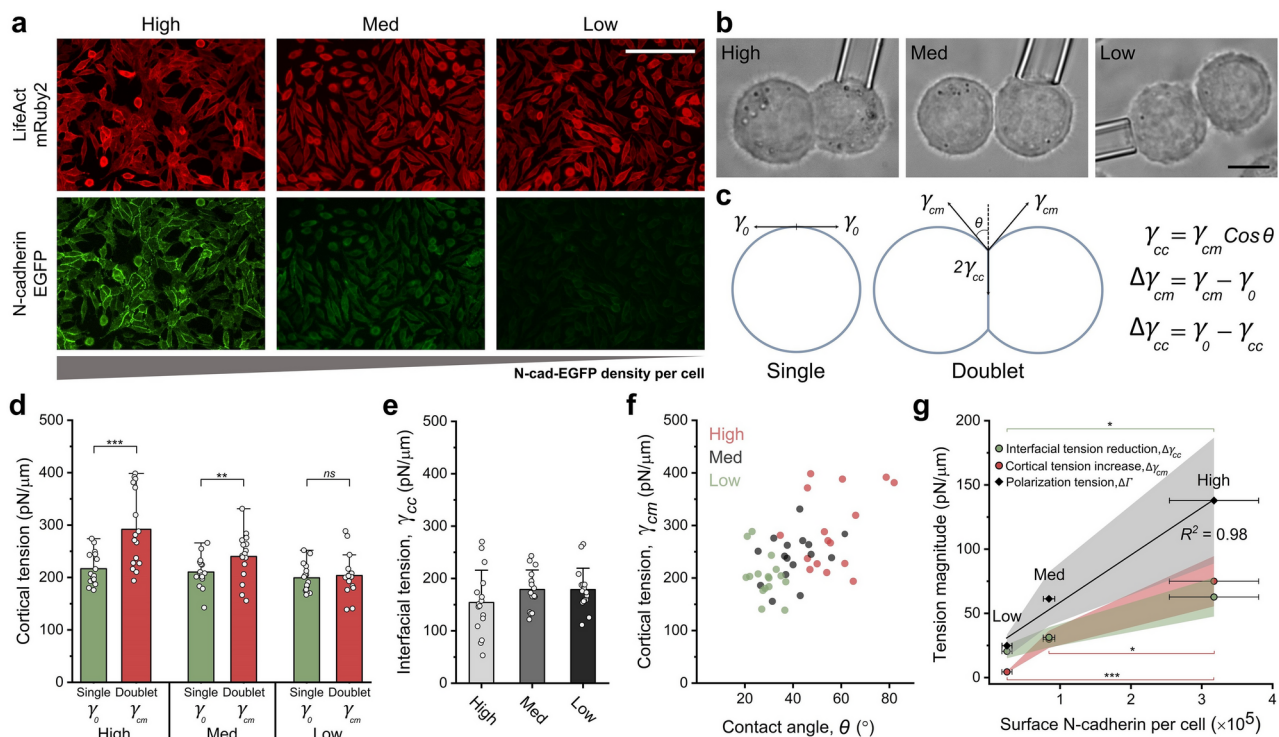
Fig. 1. Micropipette aspiration for cortical tension quantification. (**a**) A schematic of the aspiration process for a single suspended cell. An aspiration pressure, $\triangle P$, in the range of 40-250 Pa is applied to deform the F-actin cortex. The Young-Laplace equation is used to extract cortical tension. R_p is the micropipette radius, R_c is the cell radius, L_p is the length of cell aspirated into the micropipette, and γ_0 is the cortical tension for single suspended cells. ΔP_{cr} is the pressure when $L_p = R_p$ is reached. (**b**) A single engineered L929 cell expressing a relatively high level of N-cadherin receptors (LAN-High) and undergoing aspiration was observed in bright-field, RFP, and GFP channels. Arrowheads indicate the aspirated region. Scale bar is 10 μm. (**c**) An example of the applied aspiration pressure profile with 30-sec hold time (left axis) and the corresponding evolution of the normalized protrusion length, L_p/R_p (right axis); $n = 5$. (d) Dependence of cortical tension measurement on the hold time. $n = 16$ for 10, 20, and 30 s; $n = 9$ for 60 s.

We quantified tension changes in comparison with single cells in Fig. 2g. Tension increase at the cell-medium interface is denoted by $\Delta\gamma_{cm}$, which is the difference between γ_{cm} and γ_0. Tension reduction at the cell-cell contact is denoted by $\Delta\gamma_{cc}$, computed as $\gamma_0 - \gamma_{cc}$ to maintain a positive magnitude (see Fig. 2c). Fig. 2g shows that both are strongly correlated with the surface cadherin number ($\Delta\gamma_{cc}$ is linearly dependent on N-cadherin density, whereas $\Delta\gamma_{cm}$ shows linear correlation with N-cadherin density on a semi-log scale; see Fig. S1). Their sum equals $\gamma_{cm} - \gamma_{cc}$, which we denote by $\Delta\Gamma$ and term "polarization tension" and also show in Fig. 2g. This quantity is often used to estimate TST[18], and is also linearly correlated with the expression of N-cadherins per cell (further discussed in the Discussion section). Together, these results affirm that N-cadherin-based adhesion both upregulates contractility away from contact surface and down-regulates tension at the contact surface. Further, the regulation strength is proportional to cadherin surface density per cell. In other words, N-cadherin regulates tension polarization in a strongly density-dependent manner. It is important to note that while our diffraction-limited images suggest N-cadherin distributes homogeneously on the cell surface (see Fig. 1b), nanoscale heterogeneity in N-cadherin density could exist.

The magnitude of tension polarization can be quantified with the normalized tension polarization factor, $\mathcal{P}$:

$$\mathcal{P} = \frac{\gamma_{cm} - \gamma_{cc}}{\gamma_0} = \frac{\triangle\gamma_{cm}}{\gamma_0} + \frac{\triangle\gamma_{cc}}{\gamma_0}.$$

Not surprisingly, this factor is equivalent to the leading order (via a Taylor expansion, see SI) with the so-called adhesiveness factor, $1 - \cos\theta$, which is a simple geometric quantifier for the strength of adhesion as it increases monotonically with the contact angle, θ[19]. The first term in the equation represents the contribution in tension polarization due to contractility upregulation at the cell-medium boundary, whereas the second term represents interfacial tension reduction. Table 1 summarizes the results for the individual terms as well as their relative contribution to tension polarization factor/adhesiveness. As the strength of N-cadherin-based adhesion increases, both contributions increase in absolute magnitude. However, the relative contribution of contractility

Fig. 2. Tension regulation via cell-cell adhesion is proportional to the N-cadherin expression level. (**a**) Fluorescence images of engineered cell lines expressing LifeAct-mRuby2 (top) and N-cad-EGFP (bottom) show relatively constant levels of actin and an increase in the expression of N-cadherins from right to left respectively. Scale bar is 50 μm. (**b**) Doublets of LAN-High, LAN-Med, and LAN-Low cell lines under aspiration 1 hour after contact formation. The difference in contact angle is evident between cell lines. Scale bar is 10 μm. (**c**) A schematic of the physical model to compute various tension quantities. γ_0 and γ_{cm} are tension at the cell-medium interface for single cell and doublet, respectively. γ_{cc} is interfacial tension, and θ is contact angle. $\Delta\gamma_{cm}$ and $\Delta\gamma_{cc}$ quantify tension increase at the cell-medium interface and decrease at the cell-cell interface, respectively. (**d**) Comparison of cortical tension between single cells and doublets, and (**e**) interfacial tension for the 3 cell lines. $n = 16$ for each group. (**f**) Correlation between cortical tension and contact angle in doublets for each cell line. $n = 48$, Pearson Coefficient = 0.55, $p = 4 \times 10^{-5}$. (**g**) All tension changes (at cell-medium and cell-cell interfaces and the polarization tension) strongly depend on N-cadherin receptor density per cell. The colored regions indicate SE, $^*p < 0.05$, $^{**}p < 0.01$, $^{***}p < 0.001$.

Parameter	LAN-Low	LAN-Med	LAN-High
$\langle \Delta\gamma_{cm} \rangle / \langle \gamma_0 \rangle$	0.02	0.14	0.35
$\langle \Delta\gamma_{cc} \rangle / \langle \gamma_0 \rangle$	0.10	0.15	0.29
$\langle \mathcal{P} \rangle$	0.12	0.29	0.64
Cortical tension increase contribution	17%	48%	54%
Interfacial tension reduction contribution	83%	52%	46%

Table 1. Relative contribution of cortical tension increase ($\Delta\gamma_{cm}$) and interfacial tension reduction ($\Delta\gamma_{cc}$) to tension polarization factor for the different N-cadherin expression levels. $\langle \cdot \rangle$ denotes group average.

increases, from just 17% for LAN-Low to 48% for LAN-Med, and further to a significant 54% for LAN-High. These results indicate that N-cadherin molecules are responsible for the upregulation of actomyosin-derived contractility at the external boundary of cells.

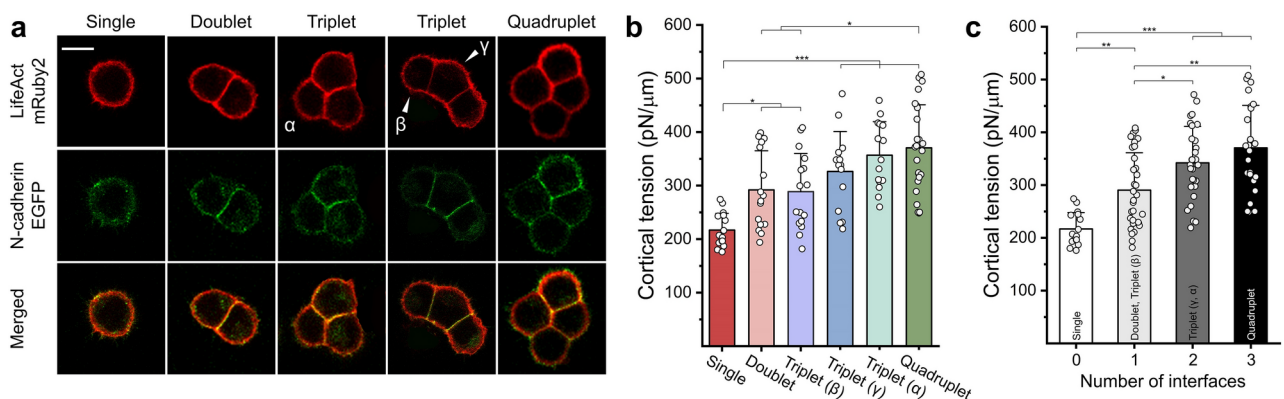## Tension polarization is further enhanced in multiplets

We further investigated adhesion-tension coupling with a greater number of cells, which is important in understanding the collective behavior of cells in various contexts[10,11,18]. We measure tension in groups of three (triplets) and four (quadruplets) LAN-High cells adhered together. Cells in triplets were categorized and labeled based on their conformation (Fig. 3a): an α-cell has two contiguous cell-cell interfaces with two neighboring cells; a β-cell has only one neighbor hence one cell-cell interface; and a γ-cell has two neighbors and cell-cell interfaces on each side, discontiguous with each other. For quadruplets, only cells with 3 interfaces (neighbors) were probed. This is due to substantial number of different arrangements for cells in this conformation that this paper does not intend to exhaust. Figure 3b shows tension measurement based on interfacial conformation. While doublets demonstrate tension increase compared to single cells, which we have already shown, cortical tension varies significantly among triplet groups. The β group (with only one cell-cell interface) shows similar mean and distribution of tension values compared with doublets. On the other hand, triplet cells with two interfaces (α and γ) exhibit higher tension and also have a similar distribution to each other. Last but not least, measured quadruplet tension values are higher on average than all others, but with no established statistical significance when compared with the α and β groups. The p-values evaluated by Tukey's HSD test are listed in Table S1.

These observations led us to hypothesize that cortical tension is influenced more by the number of interfaces than their group size. We thus re-group data based on such and show the results in Fig. 3c, where "0" includes all single cells; "1", β-cells; "2", α- and γ-cells; and 3, cells with three contiguous cell-cell interfaces in a quadruplet. The trend of tension increase along with more cell-cell interfaces becomes evident. Details of p-values between each group evaluated by Tukey's HSD test are denoted in Table S2.
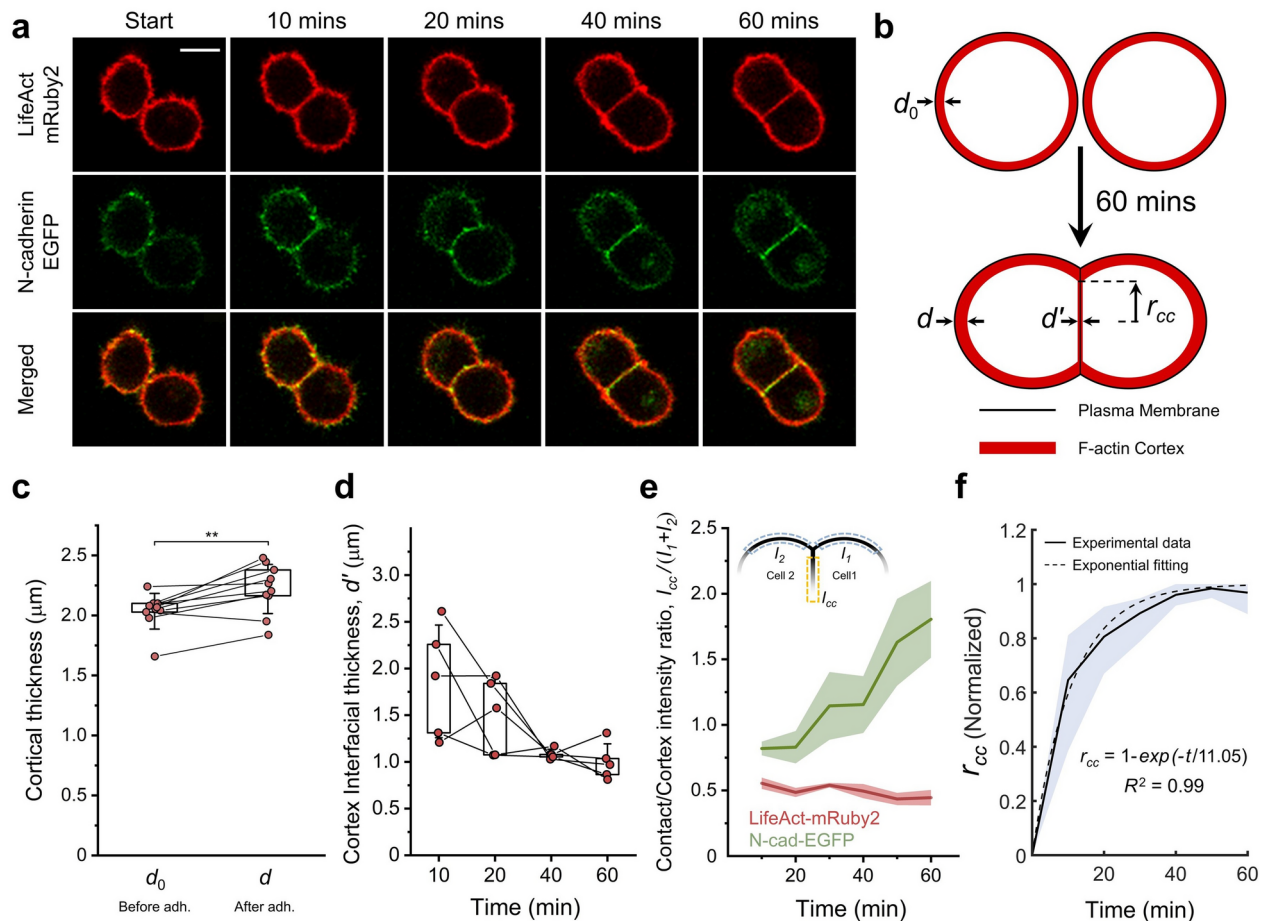
F-actin cortex and N-cadherin reorganization during contact formation

We next examine cytoskeletal remodeling during contact formation and tension polarization. Figure 4a shows representative images of *de novo* doublet formation with two LAN-High cells. The reorganization of the F-actin cortex and localization of N-cadherin clusters are quantified throughout the adhesion maturation. Indeed, the observed increase in cortical tension in the previous sections is corroborated with an increase in the thickness of the F-actin cortical bundle at the cell periphery. The thickness of the F-actin ring was measured using a custom image processing method at different locations over time. Cortical thickness is measured at the non-contacting regions prior to adhesion (d_0) and at 1-hour post-adhesion start (d). A schematic of actin cortex remodeling during the adhesion propagation is illustrated in Fig. 4b. On average, the cortical thickness is 10% higher in cells after adhesion maturation (Fig. 4c, $p = 0.003$), which correlates with a 35% increase in tension at that region. Simultaneously, the actin cortex undergoes thinning in the cell-cell contact region, facilitating adhesion expansion by lowering the local tension in that region, supporting earlier studies[24,25,31,49]. The cortex interfacial thickness, d', diminishes by 47% on average after 1 h (Fig. 4d). The fluorescence intensity of LifeAct-mRuby2 at the contact region normalized by that at the cell-medium interfaces is stable with time as shown in Fig. 4e. It is important to mention that our characterization of cortex thickness is based on a specific definition outlined in the methods section, which slightly differs from that in conventional approaches[50]. While this method yields typically higher cortex thickness values than those commonly reported, the relative changes across different conditions remain informative and quantitatively meaningful.

Figure 4a also demonstrates an increased GFP intensity in the cell-cell interface over time, in line with earlier reports[17,24,31,51]. This indicates enrichment of N-cadherin-EGFP receptors as they anchor on two adjacent cells, which is quantified in Fig. 4e. The trans-dimerization of N-cadherin molecules releases free surface energy and activates the downstream pathways that lead to dynamic actin rearrangement[28]. This, in turn, results in noted tension changes in cortical and interfacial tensions, and consequently contact expansion, which is characterized

Fig. 3. Tension polarization in multiplets. (**a**) Confocal microscopy images of LAN-High cell multiplets in various topological configurations. Scale bar is 10 μm. Measured cortical tension for single and multiplets of LAN-High cells are shown with respect to (**b**) group size, and (**c**) number of cell-cell interfaces. The sample sizes are: $n = 16$ for single, doublet, and β-triplet; $n = 14$, γ-triplet; $n = 15$, α-triplet; $n = 26$, quadruplet; $n = 16, 32, 29, 26$ for cells with 0, 1, 2, and 3 interfaces, respectively. *$p < 0.05$, **$p < 0.01$, ***$p < 0.001$.
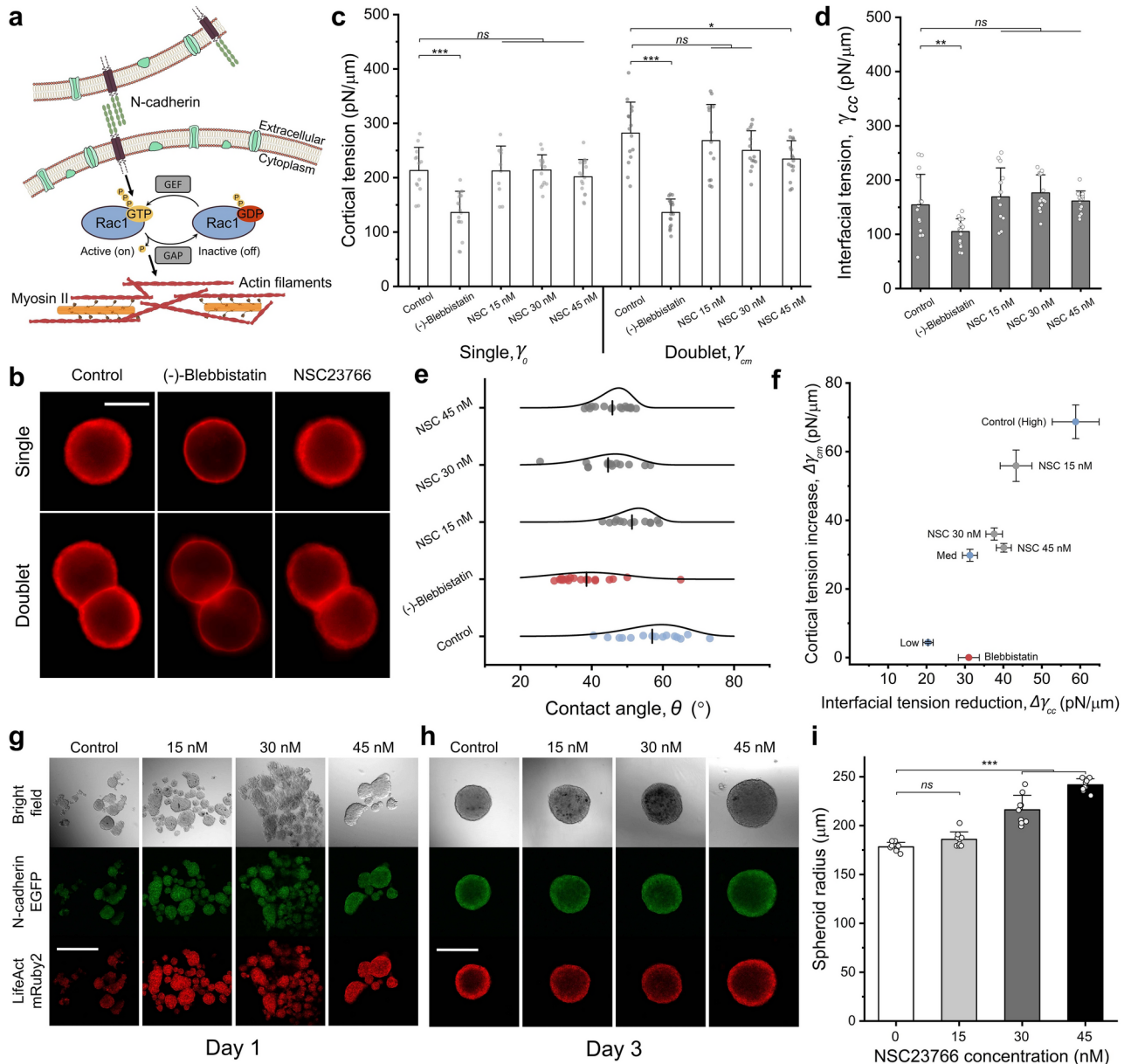
Fig. 4. Dynamic changes in actin cortical layer and N-cadherin distribution during cell-cell adhesion expansion. (a) Time-lapse confocal microscopy images of a *de novo* doublet formation with LAN-High cells captured in GFP and RFP channels. No further changes were observed after 1 hour. Scale bar is 10 μm. (b) Schematic illustration of F-actin cortex remodeling during cell-cell adhesion; cortex thickness is denoted by d_0 before adhesion and by d and d' after adhesion maturation in cell-medium and cell-cell interfaces, respectively. r_{cc} represents the radius of the contact circle. (c) Cortical thickness before (d_0) and 1 hour after (d) adhesion, $n = 10$. (d) Change in d' during contact expansion. (e) Fluorescence intensity ratio between cell-cell contact and contact-free regions for both N-cad-EGFP and LifeAct-mRuby2 proteins during the adhesion process, $n=5$. (f) Change in r_{cc} during contact expansion. The colored regions and error bars indicate SD, $n = 5$. *$p < 0.05$, **$p < 0.01$, ***$p < 0.001$.

by an increase in radius of the contact circle between cells, r_{cc} (Fig. 4f). The expansion of r_{cc} over time can be fitted with an exponential function, which suggests that cells involved in cell-cell interactions of this nature exhibit rheological properties analogous to that of highly viscous liquid droplets under the effect of surface tension[52], revealing the essence of similar patterns to those observed in the fusion of spheroids[53]. Taking together, N-cadherin recruitment led to both cortex thinning at the contact interface and thickening at the cell-medium interface, resulting in the respective tension changes[50].

Actin-N-cadherin linkage by Rac1 induces tension polarization in cells through myosin II

We next tackle the molecular pathways responsible for tension polarization in N-cadherin-based adhesion. The Rho family of small GTPases has been linked to various cellular processes that depend on dynamic cytoskeletal changes, including lamellipodia activity, myosin II-mediated contraction, cell migration, and cell-cell adhesion[21,31,54,55]. Activation of Rac1 induces interactions between the cadherins and actomyosin protein complexes, leading to changes in cellular mechanics[22]. Here we investigate the role of cytoskeletal protein components and the corresponding signaling pathways linking N-cadherin to the F-actin network. We quantify changes in tension in doublets of LAN-High cells with respect to single cells under various pharmacological treatments; untreated cells were used as control. We treated LAN-High cells with 50 μM of (-)-blebbistatin, an inhibitor of myosin II ATPase that reduces actomyosin contractility[56]. Moreover, we used various concentrations of the NSC23766 (abbreviated as NSC) to inhibit Rac1 activation (two-dimensional IC$_{50}$=30 nM, see Fig. S5a) without RhoA attenuation[57]. Extracellular dimerization of N-cadherin activates Trio, the guanine nucleotide exchange factor (GEF) for Rac1[58]. Rac1 activation modulates actin dynamics and cytoskeletal rearrangement

through interactions with downstream effectors and signaling pathways[59]. In effect, NSC decouples the Rac1-dependent molecular pathway between N-cadherin and actin by interfering with the interaction between Rac1 and its GEF[60,61]. Figure 5a shows the molecular pathways and protein complexes involved in the process.

Figure 5b demonstrates the effects of treatment with 50 μM blebbistatin and 30 nM NSC on F-actin expression and localization. In the blebbistatin-treated group, inhibition of myosin II activity led to a significant reduction in cortical thickness in both single and doublet modes. Although the doublet appeared attached in this group, the fusion of actin cortices at the cell-cell interface, as observed in the control group, was not evident, suggesting

Fig. 5. Mechanical analysis of cells and aggregates under pharmacological treatments. (**a**) A schematic of the protein complexes and molecular pathways involved in tension polarization. (**b**) Actin cortex imaging for single and doublet LAN-High cells without or with treatments (50 μM of (-)-blebbistatin, and 30 nM NSC). Scale bar is 10 μm. Measured (**c**) cortical tension, (**d**) interfacial tension, and (**e**) contact angle for LAN-High cells. In (c) colored symbols are data, the curves are Weibull distributions, and the vertical dashes are the mean values. (**f**) Calculated cortical tension increase ($\triangle\gamma_{cm}$) vs. interfacial tension reduction ($\triangle\gamma_{cc}$) for all groups. For single cell and doublets, $n = 13$ and 15 for control; $n = 17$ and 18 for blebbistatin; $n = 10$ and 15 for 15 nM NSC; $n = 14$ and 14 for 30 nM NSC; and $n = 16$ and 16 for 45 nM NSC, respectively. (**g–h**) Formation of spheroids for LAN-High cells treated with NSC at noted concentrations on Day 1 and Day 3 on agar, respectively. Scale bars are 400 μm. (**i**) Quantified spheroid radii on day 3; $n = 8, 9, 9$, and 10 for control, 15, 30, and 45 nM NSC concentration, respectively. All the *p*-values are noted in Table S3. *$p < 0.05$, **$p < 0.01$, ***$p < 0.001$.

that the observed attachment is likely just due to N-cadherin dimerization between cells. For the NSC-treated group, no apparent difference is observed between single and doublet cells, although the cortical layer seems thicker at the cell-cell contact regions in this group.

We systematically examined changes in mechanical properties due to these treatments, and the results are shown in Fig. 5c–f and Table 2. With blebbistatin, significant decreases in cortical and interfacial tension, contact angle, and tension polarization factor/adhesiveness were observed. Importantly, upregulation of cell-medium tension ($\Delta\gamma_{cm}$) by doublet formation is absent, as seen in both Fig. 5f and Table 2. Inhibition of myosin II activity, therefore, led to complete inhibition of cortical contractility at the cell-medium interface. Tension reduction at cell-cell contact is still present, although with lesser magnitude (Fig. 5f), corroborating the role of myosin II in driving contact expansion[31,49,62].

For NSC treatments, essentially no difference was observed in cortical tension for single cells (Fig. 5c left), indicating there is no change in actin contractility. On the other hand, doublets demonstrated successive decreases in cell-medium tension with increased NSC concentration, leading to decreased tension polarization, while cell-cell tension (γ_{cc}) again maintained a degree of homeostasis (Fig. 5d). The effect is best seen in Fig. 5f, where we also plot results for (untreated) LAN-Med and LAN-Low cell lines as reference points. We can appreciate that both upregulation of cell-medium tension and down-regulation of cell-cell tension are significantly reduced by Rac1 activity inhibition. These effects consequently lead to reduced tension polarization factor/adhesiveness and relative contribution of cortical tension increase (Table 2). To summarize, Rac1 inhibition with NSC suppresses tension polarization in a dose-dependent manner by both suppressing tension upregulation at the cell-medium interface and down-regulation at cell-cell contact. This conversely verifies that tension polarization is regulated by N-cadherin-based adhesion through Rac1-dependent actin reorganization and associated myosin II activities.

Tension polarization suppression led to decreased spheroid adhesiveness

We conducted further experiments to investigate the effect of Rac1 inhibition on the mechanics of spheroids with larger cell populations. Spheroids were produced using the hanging-drop method from an initial seeding of 5000 LAN-High cells treated with specified concentrations of NSC and imaged at 48h (Day 1 on agar) and 96h (Day 3 on agar) as shown in Fig. 5g,h. Spheroids on Day 2 are shown in Fig. S5b. Although aggregation still occurred in the presence of NSC, the quantified spheroid radius values were significantly higher for treated groups compared to the control group (Fig. 5i, ANOVA: $p < 0.0001$). This indicates reduced adhesiveness resulting from tension alleviation within the formed spheroids, potentially leading to an increased proliferation rate as a result of reduced tension, all attributed to inhibition of Rac1 activities[63–65].

Although aggregation still occurred in the presence of NSC, the quantified spheroid radius values were significantly higher for treated groups compared to the control group (Fig. 5i, ANOVA: $p < 0.0001$), indicating weaker adhesiveness, tension alleviation, and potentially increased proliferation within the spheroids formed due to inhibition of Rac1 activities[63].

In the above, we selected concentrations within the range of the 2D IC_{50} concentration of NSC. We further investigated higher concentrations of NSC for spheroids as the 3D IC_{50} value is expected to be up to 1 order of magnitude higher than in 2D[66]. We performed the same assay with all of LAN-High, LAN-Med, and LAN-Low cells and with NSC concentrations up to 320 nM. The effects on spheroid growth are shown in Fig. S5c. Weak aggregation was observed for treated and untreated LAN-Low cells and LAN-Med cells at lower dosages of NSC, validating the decreased polarization/adherence in these cases. Furthermore, aggregation inhibition is evident for all spheroid groups at 320 nM of NSC.

Discussion

Our work shows, in a *quantitative* manner, tension-adhesion interplay that leads to tension polarization in multicellular entities. The study highlights that N-cadherin is intrinsically a mechanosensory receptor capable of driving tension polarization by simultaneous tension upregulation at external (cell-medium) boundaries and down-regulation at internal (cell-cell) interfaces. Corroborating with prior results[17,19,30,67], tension down-regulation at cell-cell contact is likely via signaling, not direct contribution to adhesion energy. Using the energy of $2\,k_B T$ (10^{-20}J) per N-cad homogeneous binding[68], the resulting tension reduction due to dimerization of N-cadherin molecules is 0.6, 2.1, and 8 pN/µm for LAN-Low, LAN-Med, and LAN-High cells, respectively,

Parameter	Control LAN-High	50 µM Blebbistatin	15 nM NSC	30 nM NSC	45 nM NSC
$\langle\Delta\gamma_{cm}\rangle / \langle\gamma_0\rangle$	0.32	0	0.26	0.18	0.16
$\langle\Delta\gamma_{cc}\rangle / \langle\gamma_0\rangle$	0.27	0.23	0.20	0.17	0.20
$\langle\mathcal{P}\rangle$	0.59	0.23	0.46	0.35	0.36
Cortical tension increase contribution	54%	0%	57%	50%	44%
Interfacial tension reduction contribution	46%	100%	43%	50%	56%

Table 2. Relative contribution of interfacial tension reduction ($\Delta\gamma_{cc}$) and cortical tension increase ($\Delta\gamma_{cm}$) to tension polarization factor, $\mathcal{P}$, under various pharmacological treatments. $\langle\cdot\rangle$ denotes group average.

which only accounts for a small fraction of interfacial tension reduction in our experiments (Fig. 2g). On the other hand, our observations show that the regulation of tension polarization is indeed strongly dependent on surface cadherin density for all tension changes, particularly for the relative contribution of cell-medium tension upregulation to tension polarization factor/adhesiveness. The linear dependence of polarization tension on surface cadherin density corroborates the linear dependence of TST on the same variable[14], but the underlying mechanism is density-depending signaling, not via binding energy as per DAH.

Another important finding is that more cell-cell interfaces lead to stronger tension polarization. This lends a possible and intriguing route to reconcile tension measurements on smaller clusters and larger aggregates. For example, as an estimate for TST, the $\Delta\Gamma$ value we obtained for LAN-High cells is 138 pN/μm. This value is on par with that from zebrafish progenitor cells ($\sim$200 pN/μm, estimated from the pulling force[17]), but is more than one order of magnitude below that for the LN4 cell line, which has a similar level of surface N-cadherin density (5620 pN/μm)[14]. On the other hand, both the current and prior studies measured doublets or triplets with 1 to 2 interfaces, whereas a typical surface cell on an aggregate has 5.5 interfaces[69]. Extrapolating from our results, it is possible that tension polarization continues to strengthen with the number of interfaces. In particular, this may be achieved with a significant increase in γ_{cm} while γ_{cc} maintains homeostasis. (Note similar hemostatic behavior on γ_{cc} is also observed in mouse embryo compaction; see Fig. 1e in[34]). The end result is high tension on the aggregate surface with a "soft" interior, which was predicted by our prior work[70]. Further investigations along this path, including direct quantification of cortical tension on an aggregate surface, can help clear discrepancies in this field[12,18,71].

This work evaluated actin cytoskeleton reorganization in connection with N-cadherin-mediated adhesion complexes. Our results in Fig. 4 corroborate previous studies demonstrating thinning of the cortical ring along cell-cell interface upon adhesion for contact expansion[19,24,25,31,72–74]. We also observed significant cortical thickening in non-contacting regions as a result of adhesion. Our work confirmed the ubiquitous increase of cortical thickness at the cell periphery, corresponding to higher contractility all around. Additionally, actin filaments appeared to accumulate at the rim of the cell-cell contact (see Video S1), consistent with recent observations[25,73,74]. Similarly, our work also demonstrates homogeneous N-cadherin distribution along the cell-cell contact, in contrast with reported cadherin plaque formation at the edge of the contact[5,24,31]. However, these differences might be due to those in the attached and suspended cell systems in prior and current studies, respectively[74].

Our results clearly demonstrate the crucial role of myosin II and N-cadherin-actin linkages through Rac1 in initiating contact formation, as evidenced by the effects of pharmacological treatments. Blebbistatin treatment significantly reduced the cortical tension in single cells[25,34,40,75]. Tension upregulation at the cell-medium periphery is completely annihilated, and attachment is weak, with decreased contact angle. These results again suggest that N-cadherin contribution to adhesion and contact expansion via binding energy is at best secondary. This is because in case of weakened cell-medium tension and if binding energy were a major contributor, cell attachment would be stronger instead, and contact expansion would be easier. On the other hand, myosin II inhibition also led to less interfacial tension reduction. This again corroborates the involvement of the molecule in contact expansion[31].

The highly specific Rac1 inhibition using NSC regulates the effect of N-cadherin on actin contractility, suggesting that Rac1 is a molecular switch for altering tension polarization, which is triggered and regulated by N-cadherin-based adhesion[59]. This is consistent with previous reports on the significance of Rac1 in regulating actin cytoskeletal dynamics and strengthening adhesion[27,31,76]. In this work, we have limited our investigations to Rac1, whereas the roles of the Arp2/3 complex and other members of the Rho family of GTPases, such as RhoA, quantifying the degree of contribution and the exact mechanisms by which the activation of each subgroup regulates tension polarization are also subjects of interest for further studies.

The above work has interesting implications in the context of collective migration and cancer metastasis. Although metastatic spread from solid tumors is canonically attributed to freely circulating individual tumor cells[77], the collective migration of mobile clusters of tumor cells is an under-characterized driver of deadly metastatic invasions in peritoneal tumors[10]. This effect can be partly attributed to survival-enhancing signaling that provides resistance to anoikis[78]. Peritoneal metastases show patterns of cell-adhesion molecules that are unexpected in the classical epithelial-to-mesenchymal transition (EMT) during metastasis, including increased expression of N-cadherin. This increased expression may enhance the likelihood of withstanding fluid mechanical forces and avoiding anchorage-dependent apoptosis during the metastatic journey to a distant organ. Our study sheds light on how increased expression of N-cadherin enhances the stiffness and integrity of clusters and aggregates, which may, in turn, promote metastatic spread[79]. Conversely, inhibiting N-cadherin-based tension polarization via NSC could decrease such structural integrity, inhibit small metastatic bodies from surviving within the body to re-embed elsewhere[10], and even convert solid tumors and spheroids into disaggregated single cells, as our results demonstrate. Indeed, prior works already demonstrated that NSC treatment effectively decreased the transendothelial migration of prostate cancer cells, suppressed lung tumors, and reduced cancer cell retention in bones[80,81].

Another novel perspective for cancer treatment is based on stress forecasting and alleviation in aggregates[82]. The relaxation of tension in spheroids treated with NSC could lead to a weaker diffusion barrier, allowing nutrients, wastes, and chemotherapeutic agents to flow more freely and penetrate more easily in micrometastases in peritoneal metastmetastases and solid tumors[83,84]. This suggests that combining cytotoxic treatments such as targeted chemotherapies and cell therapy methods with NSC could result in better penetration and higher cytotoxicity towards malignant cells[82,85–87].

Last but not least, although in this work we only focused on N-cadherin, the nearly perfectly linear trend between TST and cadherin density, regardless of cadherin types (N-, P-, or E-cadherin) reported by Foty and Steinberg[14] (Fig. 3 therein), suggests not only that these other (P- and E-) cadherins are equally capable of

driving tension polarization regulation, but also the *quantitative* effects could be similar, although further direct measurements of tension polarization via other subtypes of cadherins needs to be addressed in future works. Altogether the current work and prior results, which are of different cell types under different contexts, suggest that cadherin-regulated tension polarization may be a very general mechanism of action driving critical physiological processes and multicellular organization.

Methods

Cell culture

The HEK293FT (R70007, ThermoFisher) cell line (used below), na?ve L929 mouse fibroblasts (CCL-1, ATCC[88]), LN4 (high expressing N-cadherin control L929 line)[14], and all other L929-derived N-cadherin-EGFP (Lifeact-mRuby2) cell lines generated in this study were cultured using standard aseptic techniques in HEK medium (DMEM/F12 (Gibco) containing 10% Heat Inactivated FBS (Gibco) with 10 µg/ml gentamycin (ThermoFisher)) and passaged using TrypLE (Gibco) or PBS-EDTA (PeproTech) where indicated. For flow cytometry and cell counting procedures, all cells were filtered using 40 µm cell strainer (Corning).

Plasmid construction

The mouse N-cadherin-EGFP lentiviral transfer plasmid pSM1-NCD-PP (Fig. S2) was constructed by ligating (T4 DNA ligase, ThermoFisher) the NheI-mouse N-cadherin-EGFP-BsrGI (18870, Addgene[89]) TBE-agarose gel purified restriction fragment together with the similarly restricted and dephosphorylated gel purified pLJM1 backbone (19319, Addgene[90]). The ligated plasmid was transformed into the STBL3 bacterial strain (ThermoFisher) and selected for transformants on LB Agar (ThermoFisher) containing 50 µg/ml carbenicillin (Gold Bioscience). Colonies were screened with a standard colony PCR assay using CMV promoter forward and mouse N-cadherin reverse primers (Kapa 2G Robust, Roche), amplified by standard mini prep procedure (D6950-01, Omega Bio-Tek), and sequence-verified (Macrogen, Piscataway, NJ). The resulting fusion gene is 3492 bp, and encodes for a protein of 1164 amino acids with a predicted molecular weight of 128,771 Da. The sequence is available in Fig. S2.

Lentivirus packaging and transduction

The lentiviral vectors were generated using PEI-based transfection techniques essentially as described by Kuroda and coworkers[91,92]. Briefly, HEK293FT cells were passaged using TrypLE and plated in HEK medium at a density of 7×10^4 cell/cm^2 onto 100 mm cell culture grade dishes (Sarstedt, Cell+). The following day, the cultures were washed once with warmed Opti-MEM (Gibco) and left in 7 ml of the same medium containing 2% heat-inactivated FBS. The dishes were returned to incubator until transfection procedures. The plasmids were combined into a sterile 2 ml low DNA binding microtube (Sarstedt) containing Opti-MEM up to a final volume of 720 µl as follows: 10.0 µg of pSM1-NCAD-EGFP-PP or pLenti-Lifeact-mRuby2 BlastR (84384, Addgene[93]); 6.67 µg of psPAX2 (gift from Didier Trono, 12260, Addgene), and 3.33 µg of pMD2.G (gift from Didier Trono, 12259, Addgene). PEI was added to the tube at a ratio of 3.5 µl/µg of DNA and mixed vigorously for 10 seconds. The mixture was centrifuged briefly and incubated for 15 to 20 min at room temperature. The solution was then applied dropwise onto the HEK293 cells while gently swirling the medium. The plates were returned to the incubator, and the following morning the medium was changed to HEK medium containing 4 mM caffeine[94]. The next day the medium was collected (24h) and changed a second time without caffeine. The following day (48h) the medium was collected, pooled with 24h, centrifuged at $300 \times g$ for 5 min, and finally filtered using 50 ml tube top 0.45 µm PES vacuum filtration device (Corning). The medium was either used directly for transduction of L929 cells as described below or concentrated via ultracentrifugation using a swinging bucket SW-28 rotor for 2 hours at 25,000 rpm (average g force $82,700 \times g$). Lentivirus was resuspended at 1:100 v/v in PBS-EDTA (0.5 mM) containing 5% trehalose and frozen at -80°c until use.

Lentivirus transduction

The naïve L929 cells were transduced with pLenti-Lifeact-mRuby2-BlastR virus, clonally sorted as described below, and then transduced with the N-cadherin-EGFP virus (Fig. S3a). The medium was changed to Opti-MEM with 10 µg/ml gentamycin containing 8 µg/ml polybrene 1 hour before exposure to unfractionated (1:1, 1:2, and 1:3 dilutions) or concentrated lentivirus (1:50, 1:100, and 1:200 dilutions). The following day the medium was changed to HEK medium with 10 µg/ml Blasticidin (Gold Bio) or 1 µg/ml Puromycin (Sigma-Aldrich) for up to 1 week.

FACS sorting and cloning of LifeAct-mRuby2 and N-cadherin-EGFP expressing L929 cells

Blasticidin-selected LifeAct-mRuby2 labeled L929 cells were prepared as described above and sorted using a BD Biosciences Influx High-Speed Cell Sorter. The logical sorting gates were set to capture the top 5% brightest fluorescing cells which were sorted as single cells directly into 96-well dishes (BD Falcon/Corning). The following day and for up to 2 weeks, each well was manually scored for the presence of bright red fluorescence, consistent spindle-shaped cell morphology, and rapid growth. At the end of 2 weeks, 6 wells were selected for subcloning, and finally one most stable clone was chosen after several more passages (LA1). The Lifeact-mRuby2 L929 master line was used for modification with N-cadherin-EGFP lentivirus as described above, and then sorted as single cells into 96-well dishes into three groups: highest fluorescing (top 10 percentile, 90-100% by intensity); medium fluorescing (45-55%); and low fluorescing (lowest 10 percentile, 0-10%) as compared to na?ve cells. The following day and up to 2 weeks, the EGFP signal was used to score the relative fluorescence in the groups of sorted clones, along with growth and morphology. At that time, 6 clones from each group were chosen and subcloned by passaging and selection with 2 µg/ml Puromycin. One clone from each group, LA1NH21 for high-expressing, LA1NM21 for moderate-expressing, and LA1NL41 for low-expressing were selected based

on relative differences in fluorescence quantified by confocal microscopy and characterized for N-cadherin expression using FACS assay and Western blot analysis. For ease in distinguishing, we rename the cell lines LAN-High (for LA1NH21), LAN-Med (for LA1NM21), and LAN-Low (for LA1NL41) in texts and figures.

Cytometric analysis of N-cadherin-EGFP cell lines

Upon selecting the desired clones, a master bank of cells was created. All cell lines were prepared for standard FACS analysis as described above, placed into a 96-well dish, and analyzed for relative EGFP fluorescence signal strength using CytoFlex analyzer (Beckman Coulter). Fig. S3b-c demonstrate the results. The fold EGFP signal for LN4 and naïve L929 cells were similar, and this value was used to normalize the EGFP signal strength for other engineered cell lines. The median values for EGFP signal intensity of LAN-High, LAN-Med, and LAN-Low cell lines were respectively 17.1, 4.8, and 2.2 times greater than naïve L929 cells. To ensure consistency in the expression of N-cadherin-EGFP over time, the same clones were drawn upon from the master banks and re-analyzed with FACS analysis after 15 passages. The EGFP signal intensities were not significantly different than the first round of FACS analyses presented here.

Western blot analysis

Cell lines were dissociated from T75 flasks using PBS-EDTA and filtered through 40 µm mesh cell strainer into 50 ml tubes. An aliquot was mixed with Trypan Blue 1:1 v/v, counted, and the remainder centrifuged at $300 \times$g for 4 min at room temperature. The pellets were resuspended and lysed in freshly prepared 8M urea containing 40 mM HEPES (pH 7.4) and $1\times$ protease inhibitor cocktail (200×, P1860, Sigma-Aldrich) at a concentration of 10^7 cells per 750 µl. The suspension was transferred into a 1.5 ml low protein binding snap top tube, and incubated at room temperature for 2-3 min. The slurry was passed through a 21-gauge needle to shear the DNA and centrifuged for 2 min at $14,000 \times$g at $4°C$ to remove any insoluble matter. The supernatant was aliquoted into multiple tubes and stored at $-173°C$. An aliquot was diluted 1:4 to a final concentration of 2M urea and used for standard BCA protein determination assay. Proteins were resolved on 1.5 mm 15 well 4-12% SDS-PAGE precast NuPage gels at room temperature using MES buffer as described by the manufacturer (ThermoFisher). Estimates of concentration and molecular weight were made using Recombinant Human N-cadherin Fc Chimera Protein (1388-NC, R&D Systems, 5 to 80 ng/lane) and the Spectra™ Multicolor Broad Range Protein Ladder (26634, ThermoFisher, 8 µl per well), respectively. After 1 hr the gels were removed from the cassette and blotted at room temperature onto a nitrocellulose membrane at 25V/500mA (constant current and/or constant power, PowerEase 500) using semi-dry transfer apparatus (B1000, ThermoFisher) with $2.5\times$ concentrated NuPage Bis-Tris transfer buffer (NP0006, ThermoFisher) containing 10% methanol and cooled on ice. This higher concentration of salts was empirically determined to ensure quantitative transfer of high molecular weight proteins.

The nitrocellulose membranes were removed from the transfer apparatus, rinsed twice with distilled deionized water, and sealed into polyethylene bags with 5% non-fat skim milk (EMD Millipore) in TBS (Tris-Buffered Saline). The bags were taped onto a rotary shaker and incubated for 1h at room temperature at 300 RMP. The bag was cut open, solution was replaced with anti-N-cadherin (13A9 mouse monoclonal IgG1, Cell Signaling, 1:1000) or anti-Actin-HRP (D6A8 rabbit monoclonal, Cell Signaling, 1:5000), and placed to shake overnight at $4°C$ as described above. The following day the blots were washed 4 times with TBST (TBS, 0.1% Tween 20 Detergent), and those with anti-N-Cad were resealed into bags with goat-anti-mouse-HRP (1:5000, Sigma) in 1% skim milk TBS-T, while those incubated with anti-Actin-HRP were imaged using SuperSignal™ West Femto Maximum Sensitivity Substrate in a Syngene image capture system. After 1h shaking at room temperature, the N-cadherin blots were washed $4\times$ with TBST and imaged as with anti-actin blots (Fig. S3d).

Quantification of N-cadherin expression levels

Figure S3d-f shows the Western blotting and N-cadherin expression quantification results. For quantifying N-cadherin expression level, 10, 25, and 35 µg of lysate from LAN-High, LAN-Med, and LAN-Low cell lines followed by 35 µg of lysate extracted from naïve cell line were loaded, separated, and blotted by the method explained above. Figure S3d (left side) shows the N-cad-EGFP bands detected at ~130 kD and their relative changes from LAN-High to naïve L929 cell lines. On the right side, 20, 15, 10, 5, and 2.5 µg of lysate extracted from the LN4 cell line was used to construct a standard curve to relate back to N-cadherin receptors per cell as previously described[14]. The detected bands at ~100 kD indicate the native chicken N-cadherin protein without glycosylation, and the relative change of the band intensity due to the gradient of the protein loaded is recognized. The Western blotting was repeated 6 times with the same amount of loaded protein as described above. Captured images of blots were analyzed using Syngene software to quantify the detected band intensities. The signals from N-cadherin bands were normalized to actin values (Fig. S3e) and then converted to cell numbers using values determined by cell counting and BCA assay. LN4 lysate bands were quantified and analyzed in the same way described to construct the standard curve for the number of N-cad receptors per cell surface vs. band intensity (Fig. S3f). The detected N-cad-EGFP band intensities of newly transfected cell lines were located on the standard curve to determine the number of N-cad receptors. With respect to BCA assay readings, the extracted numbers for N-cadherin receptors per sample were converted to the number of N-cadherin receptors per cell surface. The results are summarized in Table 3.

Live cell confocal imaging

All subclones were cultured in a TC-treated 6-well plate (Eppendorf) as described in the cell culture section. A confluent cell layer was washed $3\times$ with Hank's Balanced Salt Solution (HBSS, Corning) containing Ca^{2+}/Mg^{2+}. Cells were detached using 0.1% trypsin/2mM Ca^{2+} treatment, which retains N-cadherin cell surface expression and functionality, allowing cells to effectively adhere after resuspension. Detached cells were centrifuged for 2

Cell line	cadherin receptor per cell surface (mean±SE)
LAN-High	317,294±63,101
LAN-Med	84,431±8187
LAN-Low	25,100±7154
LN4	225,04±7457

Table 3. Extracted numbers of N-cadherin receptors per cell surface for high, medium, and low N-cadherin expressing cell lines and LN4 cell line[14].

min at 2000 rpm (Allegra X-21, Beckman Coulter, Brea, CA). The pellet was resuspended in 3 ml of FlouroBrite DMEM medium (ThermoFisher) containing 10% heat-inactivated FBS with 10 μg/ml gentamycin. The solution was filtered using 40 μm cell strainer to remove clumps from the suspension and form a single-cell solution. The cell population was adjusted to 7×10^4 cell/ml. 1 ml of cell solution was transferred to 4-well Nunc™ Lab-Tek chamber slide (Fisher Scientific) double-coated with 75 μl of 2% PolyHEMA (Sigma-Aldrich) in methanol. The latter is to prevent cell adhesion to the substrate and ease the movement of cells in suspension. The chamber slide was transferred to a Zeiss LSM 780 confocal laser scanning microscope. An incubation chamber made in-house was set up surrounding the confocal microscope to keep the sample at 37°C and 5% CO_2 atmosphere with humidity, ensuring suitable conditions for live imaging. 40 slices of 500 nm-thick images were captured as Z-stacks every 10 minutes for 90 minutes in both RFP and GFP channels simultaneously with a $63 \times$ oil immersion objective until adhesion reached maturity, which took about 60 minutes for each set of experiments. The centermost cross-section of cells was selected for visualization and analysis in all assays. Video S1 shows the 3D reconstruction of the captured confocal images for a doublet right after the first contact (top), and after adhesion maturation (bottom) in both RFP and GFP channels.

Micropipette aspiration and imaging

Micropipette aspiration experiments were performed on a Ti2-A inverted fluorescent microscope (Nikon, Japan) equipped with two motorized 4-axes micromanipulators, and a motorized stage (PatchPro-5000, Scientifica, UK). Micropipettes were formed by pulling glass capillaries with a pipette puller (PUL-1000, World Precision Instruments (WPI), USA). The micropipette tips were cut to a 3-5 μm diameter opening and bent to ∼40? using a microforge (DMF1000, WPI). The other end of the micropipettes was linked to FlowEZ™ microfluidic flow controller (-69 mbar, Fluigent SAS, France) for pressure control and regulation. The micropipette holder location and angle were then adjusted to ensure the bent tip of the micropipette was parallel to the imaging plane. Zero pressure of the aspiration setup was calibrated before each set of experiments following the protocols described in Wang et al.[95].

Confluent cell layers were prepared, trypsinized, and centrifuged as described in the live-cell confocal imaging section. After the pellet was formed, cells were resuspended in CO_2-independent medium (Gibco) containing 10% heat-inactivated FBS and 10 μg/ml gentamycin. Resuspended cells were filtered with 40 μm mesh, and the cell concentration was adjusted to 2×10^4 cell/ml. 2 ml of solution was transferred to a 15 mm glass-bottom cell culture dish (NEST Scientific) double-coated with 150 μl of 2% PolyHEMA in methanol. The sample was placed on the inverted microscope with $100\times$ oil immersion objective (NA 1.3) equipped with a flexible collar objective heater (Olympus, MA, USA) for temperature control. The sample temperature was monitored and kept at 37 ?C using a temperature controller (UNO-T-H-CO2, OKO-Lab, USA). Suspended cells were captured at the micropipette tip by applying a small pressure (around 20 Pa), then the pressure was increased stepwise by 10 Pa steps until the deformation of the actin cortex layer was equal to the inner radius of the micropipette. To improve the visualization of cortex deformation, the aspiration process was imaged in both RFP and GFP channels, as well as brightfield. Cells selected for cortical tension measurements were monitored throughout the experiments to ensure they were not undergoing mitosis. The L929 cell line has a 24-hour cell cycle[96], which is significantly longer than the extended duration of 2–3 hours for cortical tension measurement, and reduces the potential impact of cell cycle-related variations on measurements.

Image processing methods

Cortical thickness was measured from confocal images. The procedure is described in Fig. S4. First, the center point of each cell was found by fitting a circle to the actin cortex in the RFP channel. Two points were selected outside the cell at a 10 μm distance from the cell center (P1 and P2 in Fig. S4a) to create an arch with a subtended angle of 25?. Six 10 μm lines were drawn from the cell center to the outer region within this arch, and fluorescent intensity histograms were extracted and averaged along these lines to constitute a mean intensity profile for cortical actin (Fig. S4b). The maximum intensity value, I_{max}, was found to occur at x_{max} near the cell membrane, which divides the intensity profile into inner and outer profiles. The intensity profile was fitted with an exponential decay function as:

$$I_x = \begin{cases} (I_{max} - I_{cyto})e^{-\eta_{in}(x_{max}-x)} + I_{cyto} & x < x_{max} \\ (I_{max} - I_{bg})e^{-\eta_{out}(x-x_{max})} + I_{bg} & x > x_{max} \end{cases}.$$

Here, I_{cyto} and I_{bg} are intensity values for cytoplasm and background, respectively, and η_{in} and η_{out} are inner and outer decay constants. The R^2 value of fitting indicated that the exponential decay function successfully predicts the intensity profile. The inner and outer cortical thickness, d_1 and d_2 in Fig. S4c, were numerically

estimated as the distance from x_{max} at which intensity value, I_x, drops to $(I_{max} - I_{cyto})/e$ for inner profile, and $(I_{max} - I_{bg})/e$ for outer profile. The two were then added to calculate the cortical thickness, as $d = d_1 + d_2$. The same process was repeated seven times at different locations to ensure capturing variations in actin cortical thickness. The final thickness values were evaluated by averaging all eight estimated thicknesses.

The measured cortical thickness values found for L929 cells are consistent with previous measurements for this cell line[97], although due to the unique nature of cytoskeletal networks in L929 cells, we used a different definition for cortical thickness than what is typically used. Hence, the reported thickness values are greater than the expected known range of 50-500 nm[50] (see Fig. S4).

Spheroid radius   was measured by image analysis in Fiji[98]. A polar transformation was performed for the centermost cross-section of the spheroids in the RFP channel. From this, a histogram plot was produced, giving a measurement of fluorescence intensity from the center of the spheroid to the edge. The spheroid edge was defined as the location at which a sudden drop-off was observed in intensity values.

Pipette radius was measured by extracting the intensity profile along a 12 μm straight line that was drawn vertically to the centerline of the pipette at 1 μm distance from the tip. The inner edges of the pipette were defined by identifying the sharp intensity difference between the white region of the pipette body and its black inner shadow. The pipette radius was determined by measuring the distance between the edges.

Contact angle, cell radius, and fluorescence intensities   were measured using Fiji and its plugins.

Pharmacological reagents

(-)-Blebbistatin (B0560, active Blebbistatin, Sigma-Aldrich) 15 mM stock in DMSO was diluted to 50 μM in CO_2-independent medium containing 10% heat-inactivated FBS and 10 μg/ml gentamycin before each set of experiments. Cells were resuspended and kept in this medium for 10 minutes. Then, samples were prepared for micropipette aspiration assays as described above.

NSC23766 (553502, VWR) 250 μM stock in DMSO was diluted to the indicated concentrations in DMEM-F12 and/or CO_2-independent medium containing 10% heat-inactivated FBS and 10 μg/ml gentamycin. For 2D cultures and micropipette aspiration assays, cells were incubated with this medium 24h prior to experiments, and the samples were prepared as described above. For spheroid assays, NSC23766 was added to the medium from the first resuspension.

NSC23766 sensitivity assay

Cells were plated at 10^5 cell/well in a 96-well plate in complete medium containing NSC23766 at indicated concentrations. At 5 days, cell viability was assayed with PrestoBlue reagent (A13261, ThermoFisher). Medium was removed and replaced with complete medium with 1:10 PrestoBlue reagent and incubated at $37°C$ for 90 minutes. Absorbance was read using a plate reader at 570 nm with the reference wavelength of 600 nm. Readings were normalized against the medium-only control. IC50 values were calculated using nonlinear regression in GraphPad Prism (Fig. S5a).

Spheroid assays

Spheroids were generated using the hanging drop method. Cells were trypsinized and resuspended in complete medium with 2 mM Ca^{2+} at 5×10^5 cell/ml. 10 μl droplets were deposited by multichannel pipette on the lid of a 96-well plate, which was then inverted over wells containing 50 μl PBS. After 48h, the 96-well lids were transferred to plates containing 50 μl complete medium over 50 μl agar and centrifuged for 1 minute at 100×*g* to transfer spheroids into wells. Spheroid plates were placed on a rotational rocker in an incubator for 72h and imaged as Z-stacks at 24h, 48h, and 72h with confocal microscopy using 10× objective to observe aggregation dynamics. The centermost image from each z-stack was selected.

Statistical analysis

All the statistical analysis was performed using MATLAB (MathWorks, Natick, MA), OriginPro 2021 (9.8.0.200, OriginLab, Northampton, MA), and GraphPad Prism (9.4.0, GraphPad Software, San Diego, CA). Student's t-test, ANOVA test, and Tukey's HSD test for all figures: *$p < 0.05$, **$p < 0.01$, *** $p < 0.001$. Bar plots show mean±s.d. Error bars show s.d., whisker boxes show Min., 2nd Quartile, Median, 3rd Quartile, and Max. values. The uncertainties in measurements are noted in Table S4.

Data availability

All the collected data and developed codes in this study are available from the corresponding author on legitimate request.

References

1. Lecuit, T. & Lenne, P. F. Cell surface mechanics and the control of cell shape, tissue patterns and morphogenesis. *Nat. Rev. Mol. Cell. Biol.* **8**, 633–644 (2007).
2. Merkel, M. & Manning, M. L. Using cell deformation and motion to predict forces and collective behavior in morphogenesis. *Semin. Cell Dev. Biol.* **67**, 161–169 (2017).
3. Sugimura, K., Lenne, P. F. & Graner, F. Measuring forces and stresses in situ in living tissues. *Development* **143**, 186–196 (2016).
4. Foty, R. A. & Steinberg, M. S. Differential adhesion in model systems. *Wiley Interdiscip. Rev. Dev. Biol.* **2**(5), 631–645 (2013).

5. Vasioukhin, V. & Fuchs, E. Actin dynamics and cell-cell adhesion in epithelia. *Curr. Opin. Cell Biol.* **13**(1), 76–84 (2001).
6. Saias, L., Gomes, A., Cazales, M., Ducommun, B. & Lobjois, V. Cell-cell adhesion and cytoskeleton tension oppose each other in regulating tumor cell aggregation. *Cancer Res.* **75**(12), 2426–2433 (2015).
7. Foty, R. A. & Steinberg, M. S. Cadherin-mediated cell-cell adhesion and tissue segregation in relation to malignancy. *Int. J. Dev. Biol.* **48**, 397–409 (2004).
8. Yamamoto, K. *et al.* Dissecting the subcellular forces sculpting early C. elegans embryos. *bioRxiv* 2023–03 (2023).
9. Foty, R. A., Pfleger, C. M., Forgacs, G. & Steinberg, M. S. Surface tensions of embryonic tissues predict their mutual envelopment behavior. *Development* **122**, 1611–1620 (1996).
10. Au, S. H. et al. Clusters of circulating tumor cells traverse capillary-sized vessels. *Proc. Natl. Acad. Sci. U.S.A.* **113**(18), 4947–4952 (2016).
11. Bi, D., Lopez, J. H., Schwarz, J. M. & Manning, M. L. A density-independent rigidity transition in biological tissues. *Nat. Phys.* **11**, 1074–1079 (2015).
12. Li, R., Moazzeni, S., Liu, L. & Lin, H. Micro and macroscopic stress-strain relations in disordered tessellated networks. *Phys. Rev. Lett.* **130**(18), 188201 (2023).
13. Steinberg, M. S. Does differential adhesion govern self-assembly processes in histogenesis? Equilibrium configurations and the emergence of a hierarchy among populations of embryonic cells. *J. Exp. Zool.* **173**, 395–434 (1970).
14. Foty, R. A. & Steinberg, M. S. The differential adhesion hypothesis: A direct evaluation. *Dev. Biol.* **278**, 255–263 (2005).
15. Brodland, G. W. The differential interfacial tension hypothesis (dith): A comprehensive theory for the self-rearrangement of embryonic cells and tissues. *J. Biomech. Eng.* **124**(2), 188–197 (2002).
16. Harris, A. K. Is cell sorting caused by differences in the work of intercellular adhesion?. *J. Theor. Biol.* **61**(2), 267–285 (1976).
17. Maître, J. L. et al. Adhesion functions in cell sorting by mechanically coupling the cortices of adhering cells. *Science* **338**(6104), 253–256 (2012).
18. Manning, M. L., Foty, R. A., Steinberg, M. S. & Schoetz, E. M. Coaction of intercellular adhesion and cortical tension specifies tissue surface tension. *Proc. Natl. Acad. Sci. U.S.A.* **107**(28), 12517–12522 (2010).
19. David, R. et al. Tissue cohesion and the mechanics of cell rearrangement. *Development* **141**, 3672–3682 (2014).
20. Winklbauer, R. Cell adhesion strength from cortical tension-an integration of concepts. *J. Cell Sci.* **128**(20), 3687–3693 (2015).
21. Fukata, M. & Kaibuchi, K. Rho-family gtpases in cadherin-mediated cell-cell adhesion. *Nat. Rev. Mol. Cell Biol.* **2**(12), 887–897 (2001).
22. Ratheesh, A. & Yap, A. S. A bigger picture: Classical cadherins and the dynamic actin cytoskeleton. *Nat. Rev. Mol. Cell Biol.* **13**(10), 673–679 (2012).
23. Slováková, J. et al. Tension-dependent stabilization of e-cadherin limits cell-cell contact expansion in zebrafish germ-layer progenitor cells. *Proc. Natl. Acad. Sci. U.S.A.* **119**(8), e2122030119 (2022).
24. Adams, C. L., Chen, Y. T., Smith, S. J. & Nelson, W. J. Mechanisms of epithelial cell-cell adhesion and cell compaction revealed by high-resolution tracking of e-cadherin-green fluorescent protein. *J. Cell Biol.* **142**(4), 1105–1119 (1998).
25. Engl, W., Arasi, B., Yap, L. L., Thiery, J. P. & Viasnoff, V. Actin dynamics modulate mechanosensitive immobilization of e-cadherin at adherens junctions. *Nat. Cell Biol.* **16**(6), 584–591 (2014).
26. Wang, J. et al. Tethering piezo channels to the actin cytoskeleton for mechanogating via the cadherin-β-catenin mechanotransduction complex. *Cell Rep.* **38**(6), 110342 (2022).
27. Chu, Y. S. et al. Force measurements in e-cadherin-mediated cell doublets reveal rapid adhesion strengthened by actin cytoskeleton remodeling through rac and cdc42. *J. Cell Biol.* **167**(6), 1183–1194 (2004).
28. Maître, J. L. & Heisenberg, C. P. Three functions of cadherins in cell adhesion. *Curr. Biol.* **23**(14), R626–R633 (2013).
29. Perret, E., Leung, A., Feracci, H. & Evans, E. Trans-bonded pairs of e-cadherin exhibit a remarkable hierarchy of mechanical strengths. *Proc. Natl. Acad. Sci. U.S.A.* **101**(47), 16472–16477 (2004).
30. Youssef, J., Nurse, A. K., Freund, L. B. & Morgan, J. R. Quantification of the forces driving self-assembly of three-dimensional microtissues. *Proc. Natl. Acad. Sci. U.S.A.* **108**(17), 6993–6998 (2011).
31. Yamada, S. & James Nelson, W. Localized zones of rho and rac activities drive initiation and expansion of epithelial cell-cell adhesion. *J. Cell Biol.* **178**(3), 517–527 (2007).
32. Amack, J. D. & Manning, M. L. Knowing the boundaries: extending the differential adhesion hypothesis in embryonic cell sorting. *Science* **338**(6104), 212–215 (2012).
33. Maruthamuthu, V., Sabass, B., Schwarz, U. S. & Gardel, M. L. Cell-ecm traction force modulates endogenous tension at cell-cell contacts. *Proc. Natl. Acad. Sci. U.S.A.* **108**(12), 4708–4713 (2011).
34. Maître, J. L., Niwayama, R., Turlier, H., Nédélec, F. & Hiiragi, T. Pulsatile cell-autonomous contractility drives compaction in the mouse embryo. *Nat. Cell Biol.* **17**, 849–855 (2015).
35. Krens, S. G., Möllmert, S. & Heisenberg, C. P. Enveloping cell-layer differentiation at the surface of zebrafish germ-layer tissue explants. *Proc. Natl. Acad. Sci. U.S.A.* **108**(3), E9–E10 (2011).
36. Duguay, D., Foty, R. A. & Steinberg, M. S. Cadherin-mediated cell adhesion and tissue segregation: Qualitative and quantitative determinants. *Dev. Biol.* **253**(2), 309–323 (2003).
37. Ryan, P. L., Foty, R. A., Kohn, J. & Steinberg, M. S. Tissue spreading on implantable substrates is a competitive outcome of cell-cell vs. cell-substratum adhesivity. *Proc. Natl. Acad. Sci. U.S.A.* **98**(8), 4323–4327 (2001).
38. Stevens, A. J. et al. Programming multicellular assembly with synthetic cell adhesion molecules. *Nature* **614**(7946), 144–152 (2023).
39. Toda, S., Blauch, L. R., Tang, S. K. Y., Morsut, L. & Lim, W. A. Programming self-organizing multicellular structures with synthetic cell-cell signaling. *Science* **361**(6398), 156–162 (2018).
40. Tinevez, J. Y. et al. Role of cortical tension in bleb growth. *Proc. Natl. Acad. Sci. U.S.A.* **106**(44), 18581–18586 (2009).
41. Paluch, E., Piel, M., Prost, J., Bornens, M. & Sykes, C. Cortical actomyosin breakage triggers shape oscillations in cells and cell fragments. *Biophys. J.* **89**(1), 724–733 (2005).
42. Moazzeni, S. et al. Single-cell mechanical analysis and tension quantification via electrodeformation relaxation. *Phys. Rev. E* **103**(3), 032409 (2021).
43. Trepat, X. et al. Universal physical responses to stretch in the living cell. *Nature* **447**(7144), 592 (2007).
44. Ward, S. M. V., Weins, A., Pollak, M. R. & Weitz, D. A. Dynamic viscoelasticity of actin cross-linked with wild-type and disease-causing mutant α-actinin-4. *Biophys. J.* **95**(10), 4915–4923 (2008).
45. Brugués, J. et al. Dynamical organization of the cytoskeletal cortex probed by micropipette aspiration. *Proc. Natl. Acad. Sci. U.S.A.* **107**(35), 15415–15420 (2010).
46. Sliogeryte, K. et al. Differential effects of lifeact-gfp and actin-gfp on cell mechanics assessed using micropipette aspiration. *J. Biomech.* **49**(2), 310–317 (2016).
47. Chivukula, V. K., Krog, B. L., Nauseef, J. T., Henry, M. D. & Vigmostad, S. C. Alterations in cancer cell mechanical properties after fluid shear stress exposure: A micropipette aspiration study. *Cell Health Cytoskelet.* **7**, 25–35 (2015).
48. Liu, Y. et al. Robotic micropipette aspiration for multiple cells. *Micromachines* **10**(5), 348 (2019).
49. Hidalgo-Carcedo, C. et al. Collective cell migration requires suppression of actomyosin at cell-cell contacts mediated by ddr1 and the cell polarity regulators par3 and par6. *Nat. Cell Biol.* **13**(1), 49–59 (2011).
50. Clark, A. G., Dierkes, K. & Paluch, E. K. Monitoring actin cortex thickness in live cells. *Biophys. J.* **105**(3), 570–580 (2013).
51. Ibata, N. & Terentjev, E. M. Nucleation of cadherin clusters on cell-cell interfaces. *Sci. Rep.* **12**(1), 18485 (2022).

52. Narhe, R., Beysens, D. & Nikolayev, V. S. Contact line dynamics in drop coalescence and spreading. *Langmuir* **20**(4), 1213–1221 (2004).
53. Kosheleva, N. V. et al. Cell spheroid fusion: Beyond liquid drops model. *Sci. Rep.* **10**(1), 1–15 (2020).
54. Ridley, A. J. Rho gtpase signalling in cell migration. *Curr. Opin. Cell Biol.* **36**, 103–112 (2015).
55. Etienne-Manneville, S. & Hall, A. Rho gtpases in cell biology. *Nature* **420**(6916), 629–635 (2002).
56. Kovács, M., Tóth, J., Hetényi, C., Málnási-Csizmadia, A. & Sellers, J. R. Mechanism of blebbistatin inhibition of myosin ii. *J. Biol. Chem.* **279**(34), 35557–35563 (2004).
57. Levay, M. et al. Nsc23766, a widely used inhibitor of rac1 activation, additionally acts as a competitive antagonist at muscarinic acetylcholine receptors. *J. Pharmacol. Exp. Ther.* **347**(1), 69–79 (2013).
58. Kruse, K. et al. N-cadherin signaling via trio assembles adherens junctions to restrict endothelial permeability. *J. Cell Biol.* **218**(1), 299–316 (2019).
59. Tejada-Simon, M. V. Modulation of actin dynamics by rac1 to target cognitive function. *J. Neurochem.* **133**(6), 767–779 (2015).
60. Gao, Y., Dickerson, J. B., Guo, F., Zheng, J. & Zheng, Y. Rational design and characterization of a rac gtpase-specific small molecule inhibitor. *Proc. Natl. Acad. Sci. U.S.A.* **101**(20), 7618–7623 (2004).
61. Yu, W., Yang, L., Li, T. & Zhang, Y. Cadherin signaling in cancer: Its functions and role as a therapeutic target. *Front. Oncol.* **9**, 989 (2019).
62. Araya, C. et al. Cdh2 coordinates myosin-ii dependent internalisation of the zebrafish neural plate. *Sci. Rep.* **9**(1), 1835 (2019).
63. Smyrek, I. et al. E-cadherin, actin, microtubules and fak dominate different spheroid formation phases and important elements of tissue integrity. *Biol. Open* **8**(1), bio037051 (2019).
64. Cheng, G., Tse, J., Jain, R. K. & Munn, L. L. Micro-environmental mechanical stress controls tumor spheroid size and morphology by suppressing proliferation and inducing apoptosis in cancer cells. *PLoS ONE* **4**(2), e4632 (2009).
65. Montel, F. et al. Isotropic stress reduces cell proliferation in tumor spheroids. *New J. Phys.* **14**(5), 055008 (2012).
66. Muguruma, M. et al. Differences in drug sensitivity between two-dimensional and three-dimensional culture systems in triple-negative breast cancer cell lines. *Biochem. Biophys. Res. Commun.* **533**(3), 268–274 (2020).
67. Rübsam, M. et al. Polarity signaling balances epithelial contractility and mechanical resistance. *Sci. Rep.* **13**(1), 7743 (2023).
68. Prakasam, A. K., Maruthamuthu, V. & Leckband, D. E. Similarities between heterophilic and homophilic cadherin adhesion. *Proc. Natl. Acad. Sci. U.S.A.* **103**(42), 15434–15439 (2006).
69. Angelov, B. et al. Nonatomic solvent-driven voronoi tessellation of proteins: An open tool to analyze protein folds. *Proteins* **49**(4), 446–456 (2002).
70. Yu, M. et al. Coherent timescales and mechanical structure of multicellular aggregates. *Biophys. J.* **114**(11), 2703–2716 (2018).
71. Li, R. et al. E 2 and gamma distributions in polygonal networks. *Phys. Rev. Res.* **3**(4), L042001 (2021).
72. Adams, C. L., Nelson, W. J. & Smith, S. J. Quantitative analysis of cadherin-catenin-actin reorganization during development of cell-cell adhesion. *J. Cell. Biol.* **135**(6), 1899–1911 (1996).
73. Yu, Q., Holmes, W. R., Thiery, J. P., Luwor, R. B. & Rajagopal, V. Cortical tension initiates the positive feedback loop between cadherin and f-actin. *Biophys. J.* **121**, 596–606 (2022).
74. de Plater, L.,Firmin, J., & Maître, J. L. Mechanical strengthening of cell-cell adhesion during mouse embryo compaction. *Biophys. J.* (2024).
75. Fischer-Friedrich, E., Hyman, A. A., Jülicher, F., Müller, D. J. & Helenius, J. Quantification of surface tension and internal pressure generated by single mitotic cells. *Sci. Rep.* **4**, 6213 (2014).
76. Ehrlich, J. S., Hansen, M. D. & Nelson, W. J. Spatio-temporal regulation of rac1 localization and lamellipodia dynamics during epithelial cell-cell adhesion. *Dev. Cell* **3**(2), 259–270 (2002).
77. Friedl, P. & Gilmour, D. Collective cell migration in morphogenesis, regeneration and cancer. *Nat. Rev. Mol. Cell Biol.* **10**(7), 445–457 (2009).
78. Capellero, S. et al. Ovarian cancer cells in ascites form aggregates that display a hybrid epithelial-mesenchymal phenotype and allows survival and proliferation of metastasizing cells. *Int. J. Mol. Sci.* **23**(2), 833 (2022).
79. Nakajima, S. et al. N-cadherin expression and epithelial-mesenchymal transition in pancreatic carcinoma. *Clin. Cancer Res.* **10**(12), 4125–4133 (2004).
80. Reymond, N., d'Água, B. B. & Ridley, A. J. Crossing the endothelial barrier during metastasis. *Nat. Rev. Cancer* **13**(12), 858–870 (2013).
81. An, N. et al. Inhibition of rac1 attenuates radiation-induced lung injury while suppresses lung tumor in mice. *Cell Death Discov.* **8**(1), 26 (2022).
82. Stylianopoulos, T. The solid mechanics of cancer and strategies for improved therapy. *J. Biomech. Eng.* **139**(2), 4991 (2017).
83. Minchinton, A. I. & Tannock, I. F. Drug penetration in solid tumours. *Nat. Rev. Cancer* **6**(8), 583–592 (2006).
84. Jang, S. H., Wientjes, M. G., Lu, D. & Au, J. L. S. Drug delivery and transport to solid tumors. *Pharm. Res.* **20**, 1337–1350 (2003).
85. Stylianopoulos, T. et al. Causes, consequences, and remedies for growth-induced solid stress in murine and human tumors. *Proc. Natl. Acad. Sci. U.S.A.* **109**(38), 15101–15108 (2012).
86. Khawar, I. A., Kim, J. H. & Kuh, H. J. Improving drug delivery to solid tumors: Priming the tumor microenvironment. *J. Control. Release* **201**, 78–89 (2015).
87. Newick, K., O'Brien, S., Moon, E. & Albelda, S. M. Car t cell therapy for solid tumors. *Annu. Rev. Med.* **68**, 139–152 (2017).
88. Evans, V. J. et al. A quantitative study of the effect of certain chemically defined media on the proliferation in vitro of strain l cells from the mouse. *J. Natl. Cancer Inst.* **13**(4), 773–783 (1953).
89. Nechiporuk, T., Fernandez, T. E. & Vasioukhin, V. Failure of epithelial tube maintenance causes hydrocephalus and renal cysts in Dlg5-/- mice. *Dev. Cell* **13**, 338–50 (2007).
90. Sancak, Y. et al. The rag gtpases bind raptor and mediate amino acid signaling to mtorc1. *Science* **320**(5882), 1496–1501 (2008).
91. Kuroda, H., Kutner, R. H., Bazan, N. G. & Reiser, J. Simplified lentivirus vector production in protein-free media using polyethylenimine-mediated transfection. *J. Virol. Methods* **157**(2), 113–121 (2009).
92. Boussif, O. et al. A versatile vector for gene and oligonucleotide transfer into cells in culture and in vivo: Polyethylenimine. *Proc. Natl. Acad. Sci. U.S.A.* **92**(16), 7297–7301 (1995).
93. Parker, S. S. et al. High fidelity cryopreservation and recovery of primary rodent cortical neurons. *ENeuro* **5**(5), 135 (2018).
94. Ellis, B. L., Potts, P. R. & Porteus, M. H. Creating higher titer lentivirus with caffeine. *Hum. Gene Ther.* **22**(1), 93–100 (2011).
95. Wang, H., Kelley, F. M., Milovanovic, D., Schuster, B. S. & Shi, Z. Surface tension and viscosity of protein condensates quantified by micropipette aspiration. *Biophys. Rep.* **1**(1), 100011 (2021).
96. Coupin, G. T., Muller, C. D., Rémy-Kristensen, A. & Kuhry, J. G. Cell surface membrane homeostasis and intracellular membrane traffic balance in mouse l929 cells. *J. Cell Sci.* **112**(14), 2431–2440 (1999).
97. MacQueen, L. A., Thibault, M., Buschmann, M. D. & Wertheimer, M. R. Electromechanical deformation of mammalian cells in suspension depends on their cortical actin thicknesses. *J. Biomech.* **45**(16), 2797–2803 (2012).
98. Schindelin, J. et al. Fiji: An open-source platform for biological-image analysis. *Nat. Methods* **9**(7), 676–682 (2012).

Acknowledgements

Author contributions

HL, SM, KKS, ZS, RIC, JDZ, and DIS conceptualized and designed research. SM, KKS, RIC, and HW performed experiments. SM, KKS, HL, and RIC analyzed data. All wrote the paper.

Declarations

Competing Interests

The authors declare no competing interests.

Additional information

Supplementary Information The online version contains supplementary material available at https://doi.org/10.1038/s41598-025-88537-9.

Correspondence and requests for materials should be addressed to Z.S. or H.L.

Reprints and permissions information is available at www.nature.com/reprints.

Publisher's note Springer Nature remains neutral with regard to jurisdictional claims in published maps and institutional affiliations.